Supporting Information for:

Control of Nanoparticle Dispersion, SEI Composition, and Electrode Morphology Enable Long Cycle Life in High Silicon Content, Nanoparticle-Based Composite Anodes for Lithium-Ion Batteries

Maxwell C. Schulze, Fernando Urias, Nikita S. Dutta, Zoey Huey, Jaclyn Coyle, Glenn Teeter, Ryan Doeren, Bertrand J. Tremolet de Villers, Sang-Don Han, Nathan R. Neale, and G. Michael Carroll*

National Renewable Energy Laboratory, 15013 Denver West Parkway, Golden, Colorado 80401, United States
*Email: mike.carroll@nrel.gov

Experimental Section

Si@PEO Synthesis and Electrode Fabrication.

Radio Frequency Non-Thermal Plasma Synthesis of Hydride-Terminated Silicon NPs. Si NPs were prepared using a custom-built RF plasma reactor, the details of which have been described elsewhere.[1] Briefly, 6.0–11.6 standard cubic centimeters per minute (sccm) of 100% silane (SiH_4), 40 sccm Ar, and 140 sccm H_2 gas flows were passed through a capacitively-coupled plasma at a pressure of 1.50 Torr in a 19 mm ID/25 mm OD quartz reactor tube. These particles exhibit a slightly higher proportion of surface silyl groups (*SiH_3) but otherwise behave equivalently in functionalization chemistry to those reported in our prior work.[2] Forward RF power of 250 W was applied at 13.56 MHz using an Advanced Energy Cesar 136 generator through an Advanced Energy VM1000 matching network (tuned to give a reflected power of 0−1 W) to a copper ring electrode giving a delivered plasma power density of 90–100 W cm^{-3}. A grounded electrode was positioned downstream and separated by 1.1–1.2 cm from the working electrode. An Advanced Energy Z'Scan device was used to dynamically monitor the plasma conditions. NPs are created in the plasma through electron impact dissociation of SiH_4 and subsequent clustering of the fragments. Single crystalline, hydrogen-terminated Si NPs were collected downstream from the plasma on a 400-mesh stainless steel filter and transferred via load-lock to an inert-atmosphere argon-filled glovebox for collection.

Radical Initiated Surface Functionalization with PEO. Surface functionalization of hydrogen-

terminated Si NP powder was carried out by heating the as prepared SiH_x-terminated silicon NPs to 175 °C while submerged in allyloxy (diethylene oxide) (PEO) with catalytic amounts (1–5 mg) of the radical-initiating agent 1,1'-azobis(cyclohexanecarbonitrile) (ABCN) while stirring for 3 d. This reaction was performed inside of an Ar-filled glove box. Following the reaction, the Si@PEO NPs were purified through centrifugation according to the following procedure: Si@PEO NPs were dispersed in toluene and then flocculated by adding hexane to the mixture, which was then centrifuged at 12,000×g for 5 min. The excess liquid was decanted. This process was performed three times, and the resulting purified Si@PEO NPs were dried to form a powder suitable for electrode slurry preparation.

Composite Electrode Fabrication. The Si@PEO NP powder was suspended in N-methyl pyrrolidone (NMP) at a 15% solid mass fraction inside of an Ar-filled glovebox. To this colloid, Timcal C45 conductive carbon powder was added. This slurry was stirred under Ar for 1 day at 100 °C. Next, a 10 wt. % solution of Ensigner Polyimide P84 in NMP was added to the mixture. The slurry was then sealed under Ar, brought outside of the glovebox and mixed using a dual axis Mazerustar planetary mixer for 90 s at rotation rate of 1400 rpm and a revolution rate of 400 rpm. The still air-free, mixed slurry was then brought back inside the glove box and was blade cast onto a copper current collector with a wet gap of 250 μm and a forward rate of 1 cm s^{-1}. The cast electrode was dried in a vacuum oven (~10^{-2} Torr) at 150 °C for 4 h. The dried electrode was then brought into ambient atmosphere where it was calendared. Finally, to thermally cure the electrodes, they were placed inside of a quartz tube in a ceramic tube furnace under 0.5 L min^{-1} flowing N_2. The electrodes were heated from room temperature to 420 °C over an hour and then held at 420 °C for 4 h. Electrode thicknesses were measured with a micrometer. The average thickness of the Cu current collector was subtracted from the thickness of the total electrode to obtain the active material thickness. Electrodes using 5.9 nm silicon that did not have PEO did not adhere to the Cu current collector and could not be assembled into a cell for comparative measurements. This poor processability is likely due to insufficient Si NP dispersion (Figure 1b) as well as highly reactive Si interfaces degrading the electrode components which is consistent with our prior reports.[3, 4]

	Surface area (m^2/mg_{Si})	Porosity	Electrode Mass Loading Range
Si@PEO	4	19%	0.6–2mg/cm^2
Si@PEO (420°C)	4	10%	0.7–2.3 mg/cm^2

Coin cell fabrication.

Half-Cells. Half-cell measurements were performed against Li-metal in a 2032 coin-type configuration. To fabricate these coin cells, a 15 mm diameter circular punch of the Si-based

composite anode was taken from the larger electrode structure. The coin cell was constructed by placing, in order: a can, washer, electrode sample, 20 µL electrolyte, d = 19 mm diameter Celgard separator (2325), 20µL electrolyte, d = 9/16" lithium metal punch (with the surface oxide layer scraped off), gasket, washer, wave spring, cup and pressing the assembly in a coin cell press. The electrolyte used for these experiments was GenF: Gen2 (3:7 w/w ethylene carbonate:ethylmethylcarbonate with 1.2 M $LiPF_6$) + 3 wt.% fluoroethylenecarbonate (FEC). The Gen2 electrolyte and FEC were purchased from Tomiyama. The cell was sealed using a Hohsen automatic hydraulic crimper and allowed to rest for two hours at open circuit prior to beginning forming cycles.

Full-Cells. All full-cell data were collected on prelithiated Si@PEO electrodes as described below. Following prelithiation, the Si@PEO electrode was harvested from the half-cell and assembled into a full-cell against one of the specified Lithium Nickle Manganese Cobalt Oxide (NMC)-based cathodes. NMC cathodes were provide by the CAMP facility at Argonne National Laboratory. The specifications for each cathode are listed in the table below. The areal capacities were determined in a half-cell configuration against Li metal using a voltage range of 3.0–4.2V. Full-cells were assembled with the following stack order: Negative cell case, coin cell gasket, 0.5 mm thick SS spacer, 15 mm diameter punch of Si@PEO electrode, 40 µL of electrolyte, 19 mm diameter punch of Celgard 2325, 14 mm cathode punch, 0.5 mm thick SS spacer, wave spring, positive cell cap. The cell was allowed to rest at open circuit for two hours to sufficiently wet the surface. The total mass considered for the cell stack energy density in Figure 6 of the main text is described below.

$$Cell\ stack\ energy\ density = \frac{Energy\ (Wh)}{Anode\ mass_{Cu + composite} + Cathode\ mass_{Al + composite} + separator\ mass}$$

Full-Cell Electrode Balancing. Capacity matching cathodes with anodes in full-cell configuration was achieved by first measuring the electrochemical capacity of the anode in a half-cell configuration. Next, the anode was prelithiated (described below). The capacity of the anode for cycling against an NMC cathodes was calculated using the measured capacity and subtracting the capacity which was used for prelithiation (18% SOC). For example, if a silicon anode displayed a reversible capacity of 2 mAh/cm^2 in a half-cell configuration and was prethiated to 18% SOC, the available capacity of the anode to cycle against an NMC cathode is 1.64 mAh/cm^2. If that electrode were paired with a cathode that has 1.5 mAh/cm^2 capacity, the *n:p* ratio we report is 1.09:1. With continual consumption of the excess Li inventory upon repetitive cycles, the prelithiated Si would deplete it's initial Li excess (18%SOC) and eventually, the *n:p* ratio would reach 1.3:1.

Active Material	Carbon	Binder	Areal Capacity (3.0–4.2V vs Li)

NMC622 (90%)	C45 (5%)	Solvay 5130 (5%)	1.58 mAh/cm^2
NMC811 (90%)	C45 (5%)	Solvay 5130 (5%)	1.66 mAh/cm^2
NMC811 (90%)	C45 (5%)	Solvay 5130 (5%)	2.55 mAh/cm^2

Electrochemical Cycling.

All electrochemical cycling was performed on a Maccor, model series 4000 and all cycling was performed in GenF electrolyte.

Half-Cell Forming Procedure. The cycling protocol consisted of three charge/discharge cycles between 1.5 and 0.01 V vs Li/Li$^+$ at a rate of C/20. C-rates were calculated based on the assumed experimental silicon capacity of 3579 mAh g^{-1} and measured C45 capacity of 120 mAh g^{-1}. Extended cycling in half-cells is prone to artifacts from the corrosive nature of the Li metal counter electrode. For this reason, we only report the first three cycles in a half-cell. Extended cycling data was all performed in a full-cell configuration.

Electrochemical Prelithiation. Si@PEO electrodes were electrochemically prelithiated by performing a lithation/delithiation electrochemical cycle at C/20 and stopping the delithiation sweep at 0.6 V vs Li/Li$^+$ (Figure S1). This prelithiation provides 18% of the total lithiation capacity of the Si@PEO electrode to compensate for irreversible losses of electroactive Li-inventory during full-cell cycling.
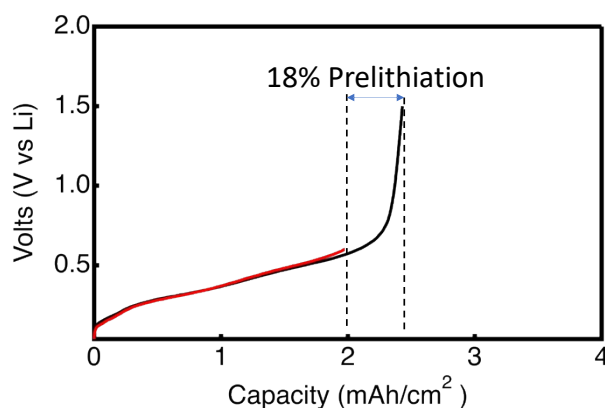

Figure S1. Voltage profile of the prelithiation protocol on the delithiation sweep. The red trace shows a voltage profile of delithiating silicon and stopping at 0.6 V. The black trace shows a voltage profile of the same electrode delithiating to 1.5 V.

Full-Cell Procedure. The full-cell cycling protocol consisted of 99 charge/discharge cycles between 4.2 and 3.0 V at a rate of C/3 followed by a charge/discharge cycle at C/10. This process was repeated 10 times to collect 1000 cycles. Performing 99 C/3 cycles may induce pore closure or generally limit Li$^+$ transport in later cycles compared to early cycles. Such an effect can

convolute irreversible processes with Li^+-transport-limited capacity. The periodic C/10 cycles are intended to delineate Li^+ transport limited capacity from irreversible processes. An increasing difference between the C/3 and C/10 cycles with continued cycled would indicate Li^+ transport bottleneck. Observing the same difference in capacity between of C/3 and C/10 cycles indicates irreversible losses. C-rates were calculated based on the capacity of the cathode which was limiting in all full-cell measurements.

Characterization.

Dynamic Light Scattering. Si@PEO and Si–SiH$_x$ particle size distribution data were collected on a Malvern Zetasizer Nano by first functionalizing the Si@PEO NPs as described above. The dried, Si@PEO powder was resuspended in NMP at a concentration of ~0.1 mg/mL by stirring the suspension while heating (100°C) under an Ar atmosphere. In the case of Si–SiH$_x$ NPs, the powder was suspended directly into NMP without chemical modification to the surface. DLS was measured of the resulting suspension.

Thermal Gravimetric Analysis. 5 mg of a powdered sample of Si@PEO NPs, the composite electrode powder, or PI were sealed into a TA Instruments Tzero DSC pan with a Tzero hermetic pinhole lid to minimize exposure of the sample to atmospheric oxygen or water during transfer to the TGA instrument located outside the glovebox. The pan and lids were tared on the TGA instrument (TA Instruments) before the sample was sealed inside. The sealed sample was equilibrated in the TGA at 50 °C and then again at 200 °C (to ensure complete removal of NMP) under flowing Ar (100 mL/min) before being ramped to 600 °C at 5 °C/min.

Scanning Electron Microscopy. All SEM images were collected using a Hitachi 4800 microscope with a 15 kV accelerating voltage and a working distance of approximately 10-12 mm. Samples for cross-sectional SEM images were prepared by tearing an electrode (either before or after electrochemical cycling). The top-down images of the electrodes were collected with no further sample preparation steps.
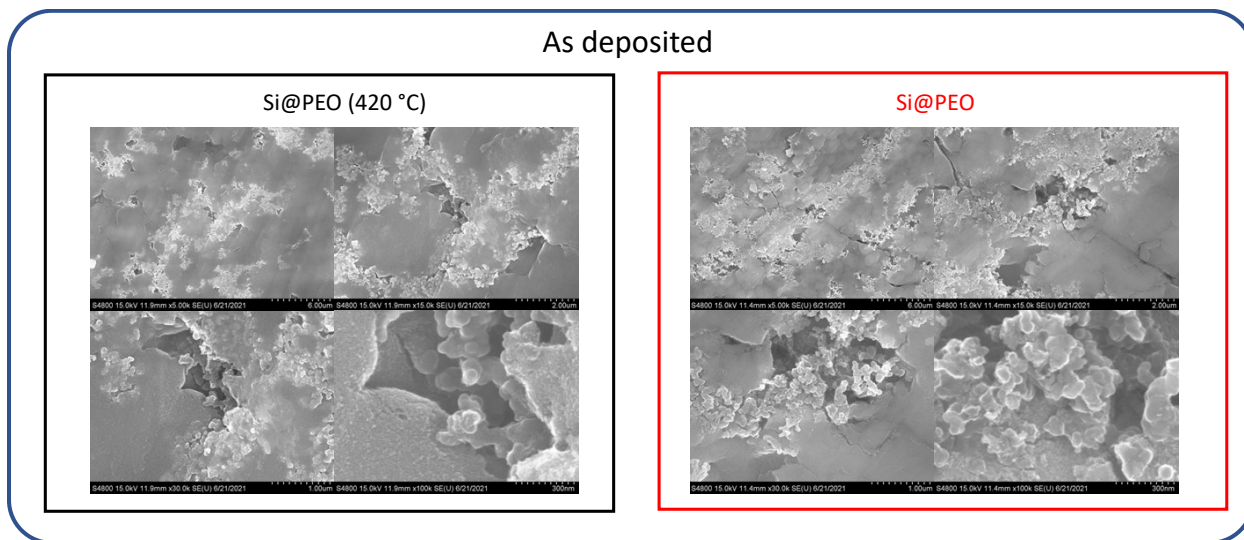
Figure S2. Top-down SEM comparison. Top-down scanning electron microscopy images at different magnifications for Si@PEO (420 °C) and Si@PEO.
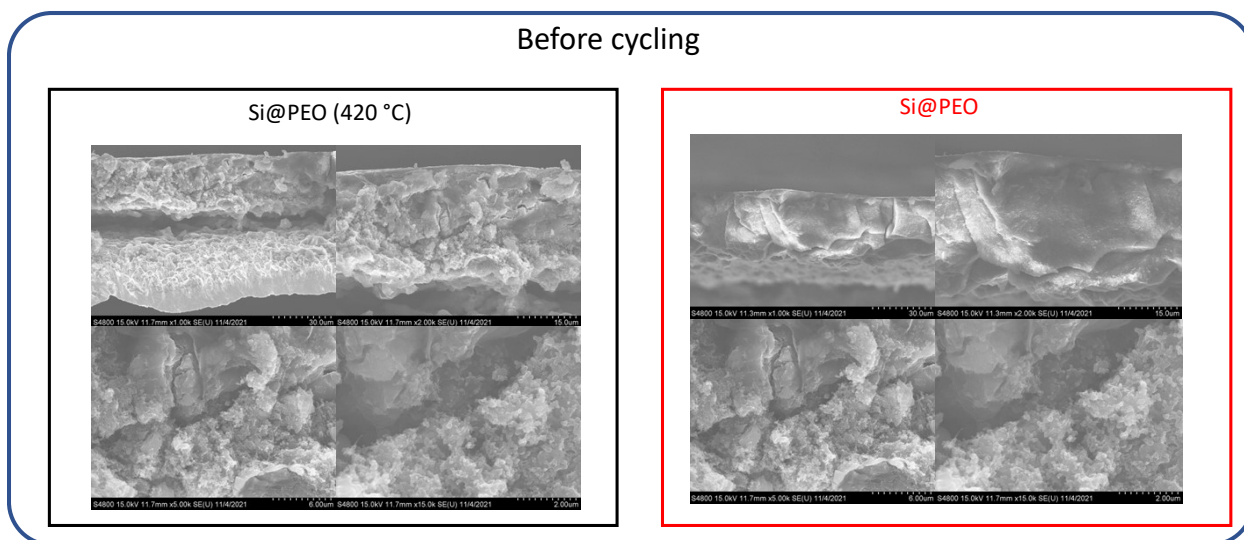

Figure S3. Cross-Sectional SEM comparison. Cross-sectional scanning electron microscopy images at different magnifications for Si@PEO (420 °C) and Si@PEO.
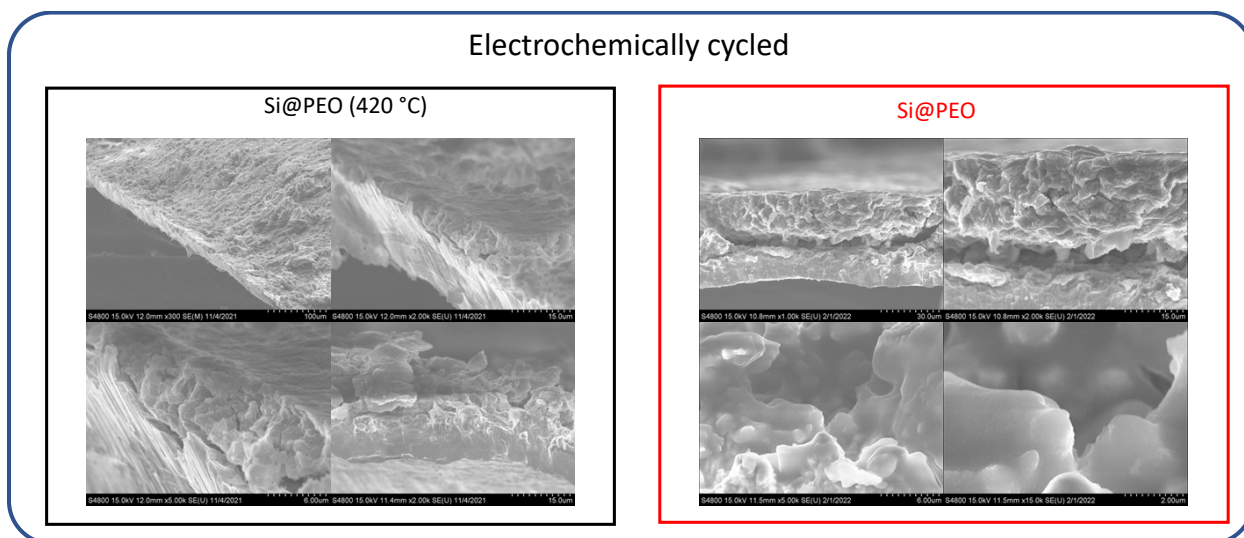
Figure S4. SEM comparison of cycled electrodes. Cross-sectional scanning electron microscopy images at different magnifications for Si@PEO (420 °C) and Si@PEO after three lithiation/delithiation cycles.

Transmission Electron Microscopy. Samples for transmission electron microscopy (TEM) were prepared in an Ar-atmosphere glovebox. Each electrode was gently scraped with a razor blade, and a copper TEM grid with lacey carbon substrate (Ted Pella) was rubbed against the surface to pick up the loosened material. Grids prepared from fresh electrodes were transferred to an FEI Tecnai ST30 TEM, operated at 300 kV. Grids prepared from cycled anodes were transferred from the glovebox to an FEI F20 S/TEM, operated at 200 kV, without air exposure using an air-free transfer holder. Size statistics were obtained using ImageJ software. Examples of the measured particle diameters are shown in Figure S5.
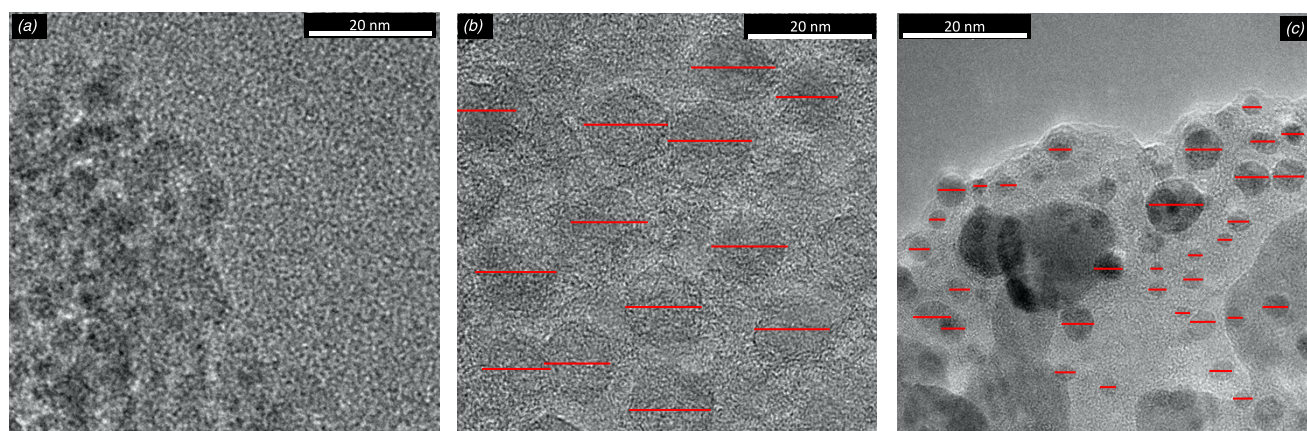

Figure S5. TEM. (a) TEM image of uncycled Si@PEO (420 °C) electrode. TEM images and examples of particle size determination of electrochemically cycled **(b)** Si@PEO (420 °C) and **(c)** Si@PEO. The red bars indicate the measured diameter of a given particle.

Scanning Spreading Resistance Microscopy. SSRM measurements were conducted on a

Bruker Dimension Icon AFM with an SSRM module, located in an Ar-filled glovebox. Bruker DDESP-V2 conductive diamond-coated probes were used to collect SSRM data in contact mode, with an applied bias voltage of –0.25 V. Cross-section samples were made by sandwiching electrodes printed on copper foil between silicon wafers with EpoTek conductive epoxy. The samples were then polished under an argon ion beam using a JEOL cooling cross section polisher.
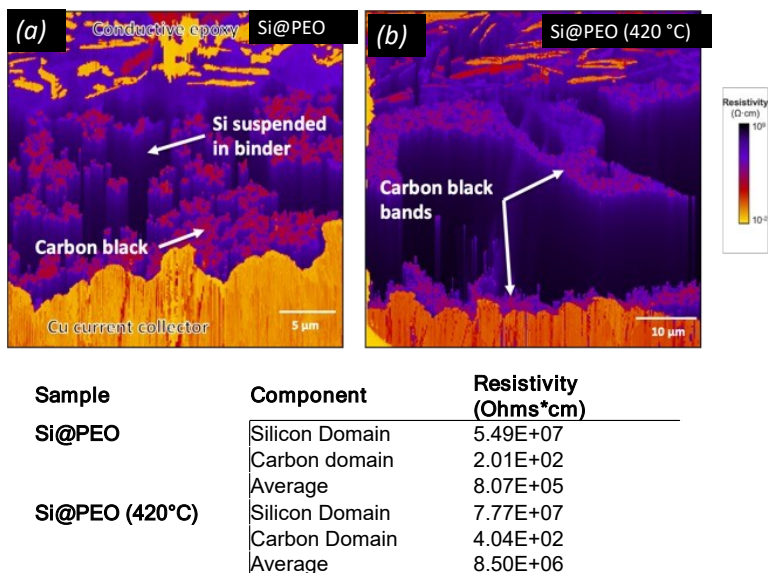

Sample	Component	Resistivity (Ohms*cm)
Si@PEO	Silicon Domain	5.49E+07
	Carbon domain	2.01E+02
	Average	8.07E+05
Si@PEO (420°C)	Silicon Domain	7.77E+07
	Carbon Domain	4.04E+02
	Average	8.50E+06

Figure S6. SSRM. SSRM cross-sectional measurement data for **(a)** Si@PEO and **(e)** Si@PEO (420 °C). The table below lists the resistivity values obtained for the specific regions identified in the SSRM image.

From SSRM cross-sectional measurements shown in Figure S6, discrete conductive carbon-rich and the silicon-rich domains are easily identified by differences in their resistivity values. Because the Si NPs are smaller than the resolution of SSRM, limited by the probe tip (~30 nm), it is likely that the PI binder, which is known to be highly resistive, impacts the resistivity measurements in the silicon domains. Upon thermal curing, the resistivities of the silicon-rich or carbon-rich domains does not change significantly in value, but there is notable segregation between the two. Where the Si NPs in the Si@PEO electrode are dispersed within the electrode bulk, the Si in the Si@PEO (420 °C) exists in distinct bands of silicon and conductive carbon. The resistivity values reported in the main text are those corresponding to the Si/binder domain. For completeness, the average resistivity (as calculated by averaging the SSRM data over the entire electrode thickness) and carbon resistivity values are also reported in the table in Figure S6.

Attenuated Total Reflectance Fourier Transform Infrared Spectroscopy (ATR-FTIR). All ATR-FTIR measurements were performed on a Bruker Alpha FTIR spectrometer equipped with either a diamond or germanium prism ATR module. Each spectrum was an average of 192 scans against a background of the argon-filled glove box. Spectra were baseline subtracted using a

convex-hull baseline fit in Igor Pro data analysis software. The spectrometer was calibrated against a polystyrene standard and the error associated with the energy accuracy is < 0.5 cm^{-1}.
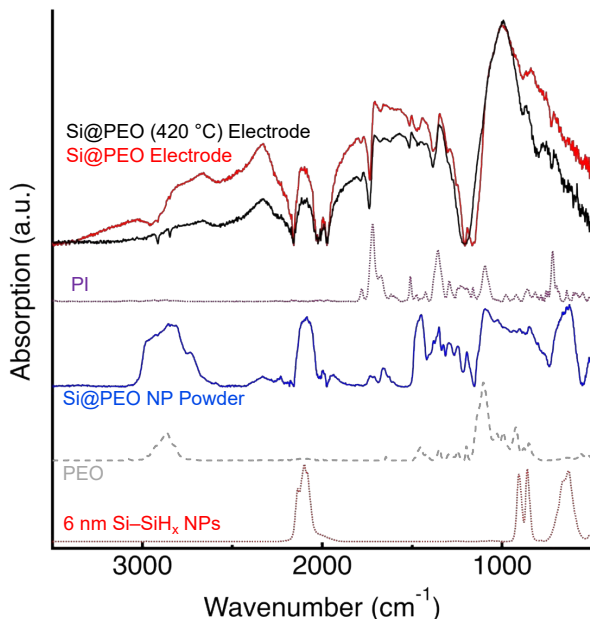

Figure S7. ATR-FTIR. Attenuated total internal reflectance (ATR) FTIR spectra for the as prepared Si–SiH$_x$ silicon NP powder (red dotted), neat PEO (grey dashed), the surface functionalized Si@PEO NP powder (blue), PI (purple dotted), Si@PEO electrode (red), and Si@PEO (420 °C) black. The spectra have been offset vertically for clarity. The spectrum of the Si@PEO electrode and Si@PEO (420 °C) are plotted on the same scale for ease of comparison.

The ATR-FTIR spectra shown in Figure S7 for the Si@PEO and Si@PEO (420 °C) electrodes display absorption features that can be attributed to one of the three components within the composite electrode. Interpretation of this spectrum is made difficult by the fact that three individual components (Silicon, PEO, and PI) have overlapping spectral signatures. However, notable differences in relative absorption between the Si@PEO and Si@PEO (420 °C) electrodes are present. For example, the absorption at 2800 cm^{-1} — attributed to C–H stretches (likely dominated by the PEO coating) — for the Si@PEO electrode spectrum is greater than the Si@PEO (420 °C) when the absorption of both electrodes is normalized to the absorption at 1000 cm^{-1} (which is attributed to absorption of the SiO$_x$). This observation is consistent with the loss of PEO and/or an increase in the SiO$_x$ content from thermal curing.

Mechanical Characterization. Nanoindentation tests were conducted using a KLA iMicro Nanoindenter equipped with a diamond Berkovich indenter tip inside an inert atmosphere glovebox. Thermal drift during indentation was maintained below 0.1 nm/s. Depth controlled tests with a constant strain rate of 0.05 s^{-1} were used with a 10 s hold at maximum load. The maximum depth was chosen such that it did not exceed greater than 1/10 the total thickness of the electrode to eliminate any effects from the copper substrate. The Oliver-Pharr method was followed to

determine the elastic modulus and hardness of the material.[5] The reported values are averages of at least 50 individual indents on each sample.
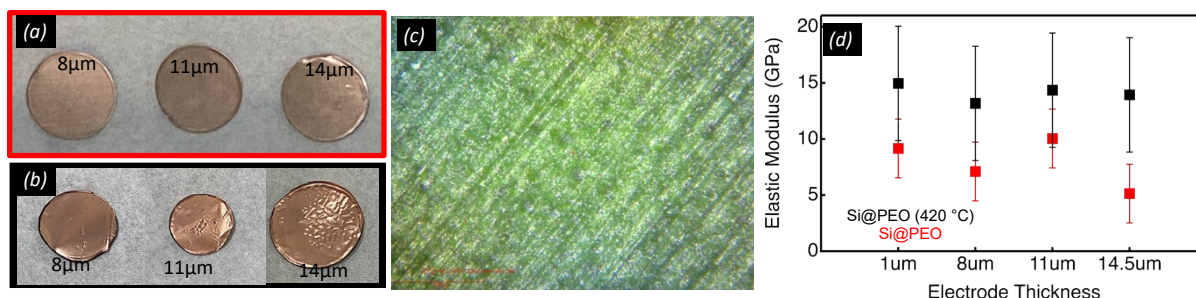

Figure S8. Mechanical characterization. Photographs of the copper current collector side of **(a)** Si@PEO and **(b)** Si@PEO (420 °C) electrodes after three electrochemical lithiation/delithiation cycles for three different electrode thicknesses (8, 11, and 14μm). The copper side of this electrode is shown face-up to highlight the deformation of the current collectors, which increase with increasing electrode thickness for the Si@PEO (420 °C). **(c)** Microscope image of nanoindentation used to measure the elastic modulus. **(d)** Electrode thickness-dependent average elastic moduli for four different Si@PEO (red) and Si@PEO (420 °C) (black) electrode thicknesses. The error bars are ± 1 σ from the mean. These electrodes were not electrochemically cycled.

Extended Half-Cell Cycling. From Figure S9, both Si@PEO and Si@PEO (420°C) display stable cycling for the first tens of cycles. After 95 cycles for the Si@PEO (420°C), the capacity rolls over, but no noticeable change it the CE is present. Because there is an infinite supply of Li⁺ and no change in the CE, the rollover is likely due to continuous electrolyte reaction with Li metal at the counter electrode. The surface of Li metal continuously reforms with each cycle exposing new reactive surface for electrolyte decomposition. This effect is expected to depend on the total charge passed. From Figure S9a, the same behavior is apparent for Si@PEO around cycle 250, which initially had less than half of the capacity of Si@PEO (420°C). To support this hypothesis, extended half-cell cycling of NMC 811 electrodes of different thicknesses (and areal capacities) but were otherwise identical in nature was performed. The data is displayed in Figure S9 c. From these data, the correlation between areal capacity and the roll-over point is clear; with increasing capacity (and thus charge passed) the roll over happens at earlier cycles. Indeed, these data suggest that extreme caution should be taken when interpreting extended half-cell cycling.
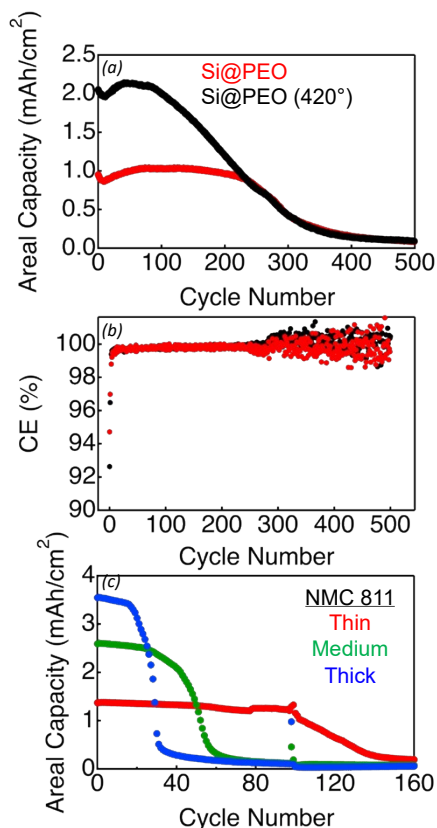
Figure S9. (a) Extended half-cell cycling of Si@PEO (red) and Si@PEO 420° (black) against Li metal as the counter electrode with GenF electrolyte. **(b)** Corresponding coulombic efficiency data for panel a. **(c)** Extended half-cell cycling data for the NMC electrodes used in this study. The thickness of the electrode is modulated of otherwise identical electrode materials. **(d)** Corresponding CE data for panel c.

Electrochemical Impedance Spectroscopy. EIS measurements were performed in a symmetric cell configuration. Prior to the measurement, two equivalent Si@PEO or Si@PEO (420 °C) electrodes were assembled into half-cells, cycled against Li to generate an SEI, and prelithiated to 0.6 V, as described above. Following these forming and prelithiation steps, the two cells were disassembled and reassembled against one another to make a single Si ‖ Si coin cell with GenF as the electrolyte. A symmetric cell configuration removes possible EIS artifacts induced by the counter/reference electrode from this two-electrode configuration. To ensure an equivalent state-of-charge, the coin cells were short circuited overnight prior to the measurement. EIS was performed on a Biologic VMP3 potentiostat using a 10 mV perturbation on top of a DC bias at 0 V. The frequency range was 10 mHz to 500 kHz. The EIS data were fit to an equivalent circuit model consisting of two parallel RC elements, a series resistor, and a Warburg diffusion element. The Nyquist plots and fits for Si@PEO and Si@PEO (420 °C) are shown in Figure S10.
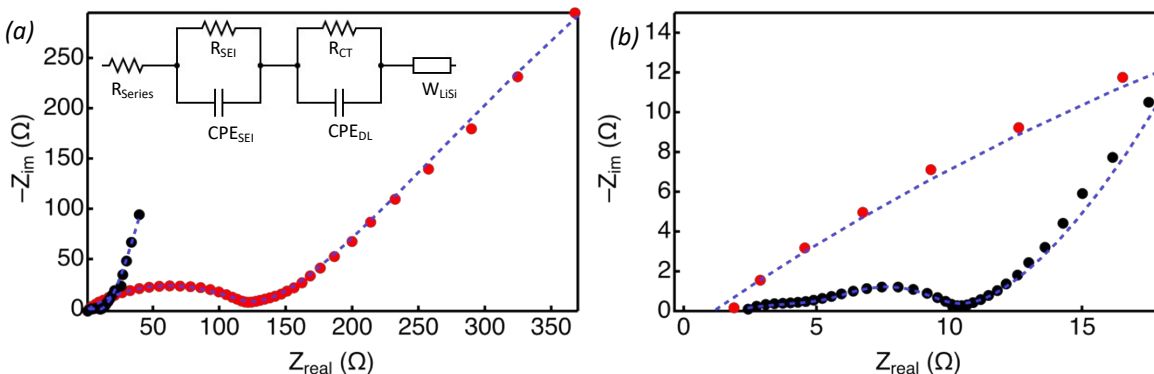
	Si@PEO	Si@PEO (420°C)
R_{CT} (Ohm)	135	2.3
CPE_{DL} (F•S^{a-1})	41e-6	7e-6
R_{SEI} (Ohm)	3441	7.1
CPE_{SEI} (F•S^{a-1})	7.6e-2	5.7e-4

Figure S10. Electrochemical Impedance Characterization. (a) Nyquist plot of Si@PEO (red) and Si@PEO (420 °C) (black) and **(b)** a zoomed in view of the same data in (a). Two Si@PEO or Si@PEO (420 °C) electrodes were first cycled in a half-cell format against Li metal in GenF electrolyte, disassembled, and reassembled in a symmetric cell configuration. The frequency range is 500 kHz to 2mHz. The blue dashed lines are equivalent circuit fits to the data.

From Figure S10 two semi-circles in the high and mid frequency range area are obvious for the Si@PEO (420 °C). These are attributed to Li$^+$ conduction and charging in the SEI and charge-transfer (CT) resistance and electric double-layer capacitance at the SEI|Si interface.[6-8] A large tail from Li^0 diffusion inside Si at mHz frequencies completes the Nyquist plots. For the Si@PEO electrode, only one semicircle is apparent. We believe that this semicircle is the CT and double-layer charging feature, but due to the thick PEO coating, the time constants of Li$^+$ transport through the SEI and SEI capacitance are similar enough that the two features overlap giving the appearance of only one semicircle.

To quantify the resistance and capacitance for each process, we fit the EIS data using the commonly invoked equivalent circuit displayed in figure S10.[8] The fit is displayed as the blue dashed line in each Nyquist plot. The values from the fits are displayed in the table below. Because of the merged semicircles for the two RC components of the Si@PEO spectrum, we do not place a high degree of confidence in the values of R_{SEI} and C_{SEI} for Si@PEO. Nevertheless, the general trends are clear and indicate an overall decrease in the cell impedance by at least one if not two orders of magnitude upon thermal curing.

X-ray photoelectron spectroscopy measurements.

XPS measurements were performed in a Physical Electronics Phi VersaProbe III instrument using monochromatic Al-ka X-rays (hν = 1486.7 eV). High-resolution spectra were acquired with a pass energy of 55 eV. Curve-fitting of XPS spectra was performed in Igor Pro

using a previously described approach where phase identification is facilitated by applying appropriate constraints on core-level binding energies and peak areas.[9]

The uncycled samples and Si@PEO powder was prepared as described above. For the cycled samples, each sample was assembled into a coin cell against Li metal, and cycled 3x at C/20 between 0.01 and 1.5 V vs Li. Once the cycled samples were finished cycling, the coin cells were disassembled, and the electrodes were rinsed in dimethylcarbonate to remove residual electrolyte. The samples were then quickly transferred to XPS vacuum to minimize sample oxidation.
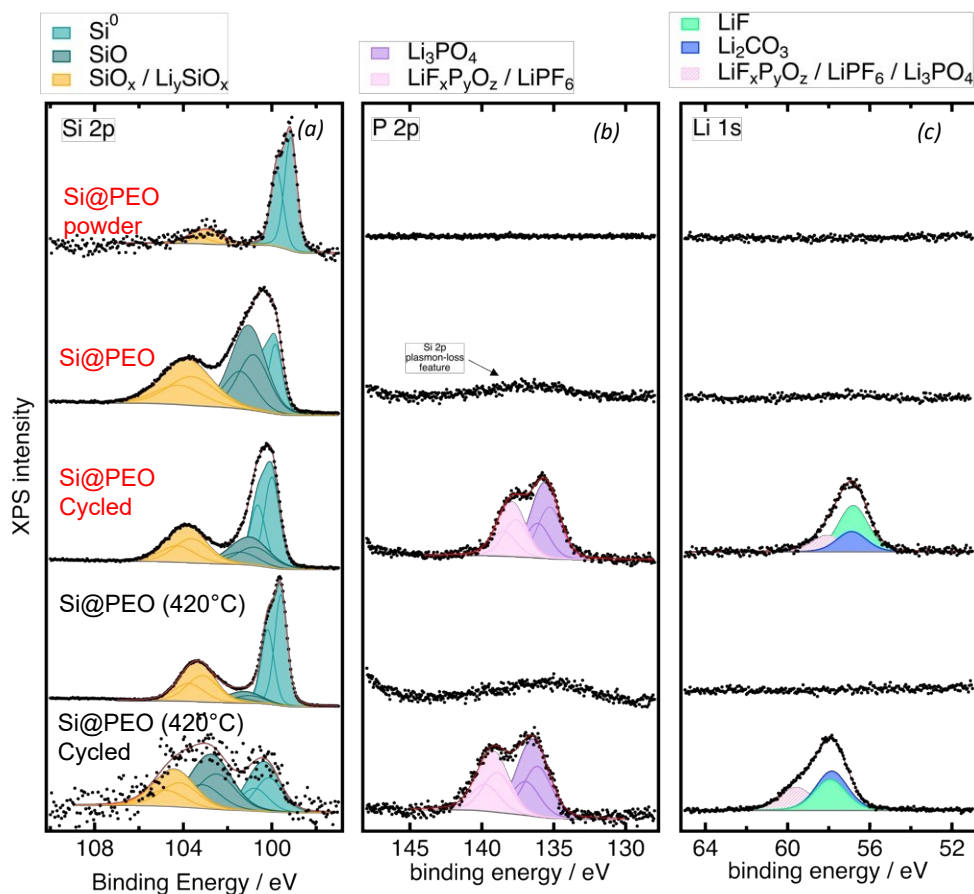

Figure S11. Additional XPS data for **(a)** Si 2p **(b)** P 2p, and **(c)** Li 1s. The fits are shown as the colored traces.

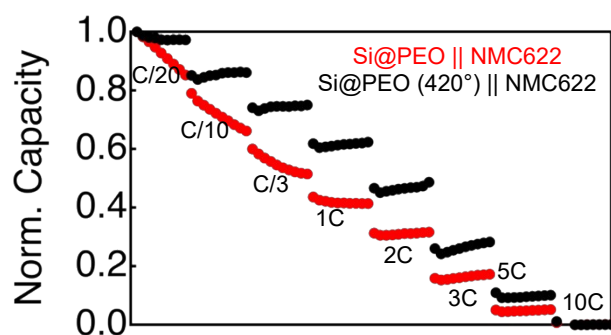**Rate Capability of Si@PEO || NMC622 and Si@PEO (420°C).**

Figure S12. Rate capability data for Si@PEO || NMC622 (red) and Si@PEO (420°C) || NMC622. The C-rate for these data were determined by the capacity of the cathode and was 1.75 mAh/cm^2.
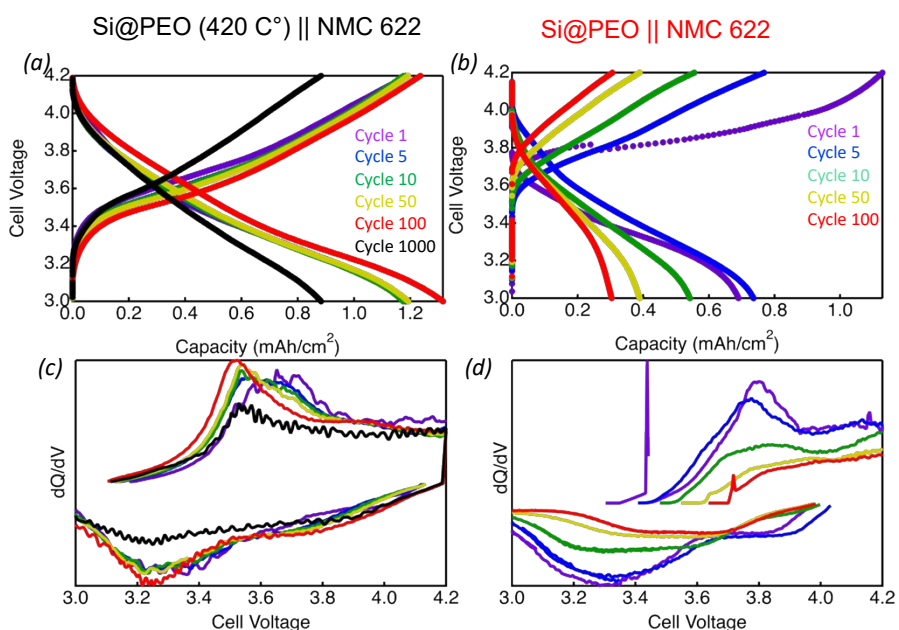
Failure Analysis of Si@PEO || NMC622.

Figure S13. Voltage profiles and differential capacity (dQ/dV) plots for **(a)** Si@PEO (420°C) || NMC622 and **(b)** Si@PEO || NMC622. The colors correspond to different cycle numbers which are indicated by the key in each plot.

Voltage profile plots in Figures S13 a and b indicate a large overpotential and poor coulombic efficiency for Si@PEO || NMC622 while the Si@PEO (420 °C) || NMC 622 cell retains most of its capacity through 1000 cycles. In agreement, differential capacity (dQ/dV) plots show that the Si@PEO (420 °C) || NMC622 electrode retains most of the voltametric shape and position throughout the 1000 cycles while Si@PEO || NMC622 shows an increasing hysteresis and

decreasing dQ/dV magnitude with increasing cycle number. The increasing hysteresis is the result of a rising cell impedance, and the decreasing magnitude is the result of a loss of active material or Li^+ inventory. The large cell impedance gain suggests blocking-type transport behavior at the electrode|electrolyte interfaces; commonly related to interfacial material accumulation. Since PEO at the Si@PEO does not accumulate with cycling, we hypothesize that material accumulation from PEO oxidation could occur at the cathode-electrolyte interface. To test this hypothesis, we performed attenuated total internal reflectance FTIR (ATR-FTIR) measurements on the NMC622 cathodes after electrochemical cycling against their respective Si-based anode. The data from those measurements is shown in Figure S12.
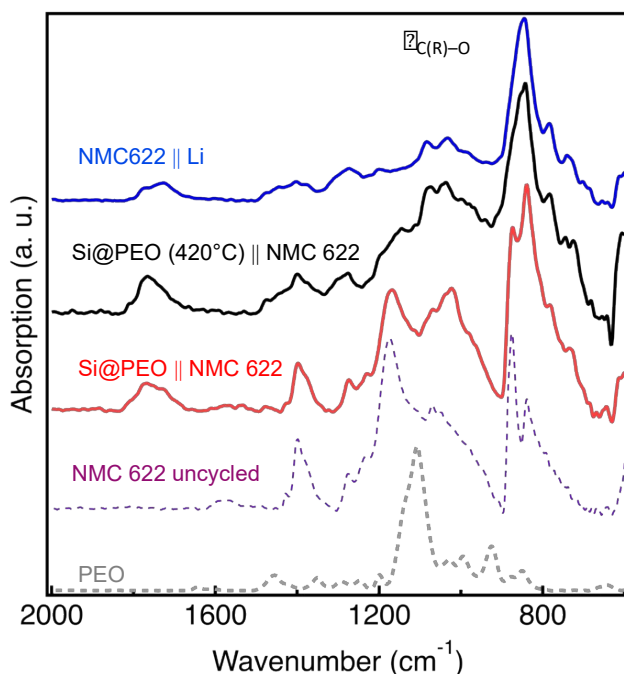

Figure S14. ATR-FTIR spectra of the NMC622 cathode (purple, dashed) and after electrochemical cycling paired against Li metal (blue), Si@PEO (420 °C) (black), Si@PEO (red). PEO is also shown for reference as the gray dashed line.

Figure S14 displays the ATR-FTIR spectra for cycled and uncycled NMC622 electrodes as well as the spectrum for PEO. The ether C–O stretch at 1150 cm^{-1} is characteristic of PEO. Comparing the Si@PEO || NMC622 against the other NMC622 spectra, an additional absorption feature is present at 1100 cm^{-1}, but because of the overlap with other spectral features in that range, it is not possible to conclusively assign that absorption feature to PEO at the NMC622 surface. SEM images of the same electrodes (Figure S13), display no notable differences between Si@PEO || NMC622 and Si@PEO (420°C) || NMC622. Indeed, even after 1000 cycles, the microstructure of these electrodes still resembles the pristine NMC622.
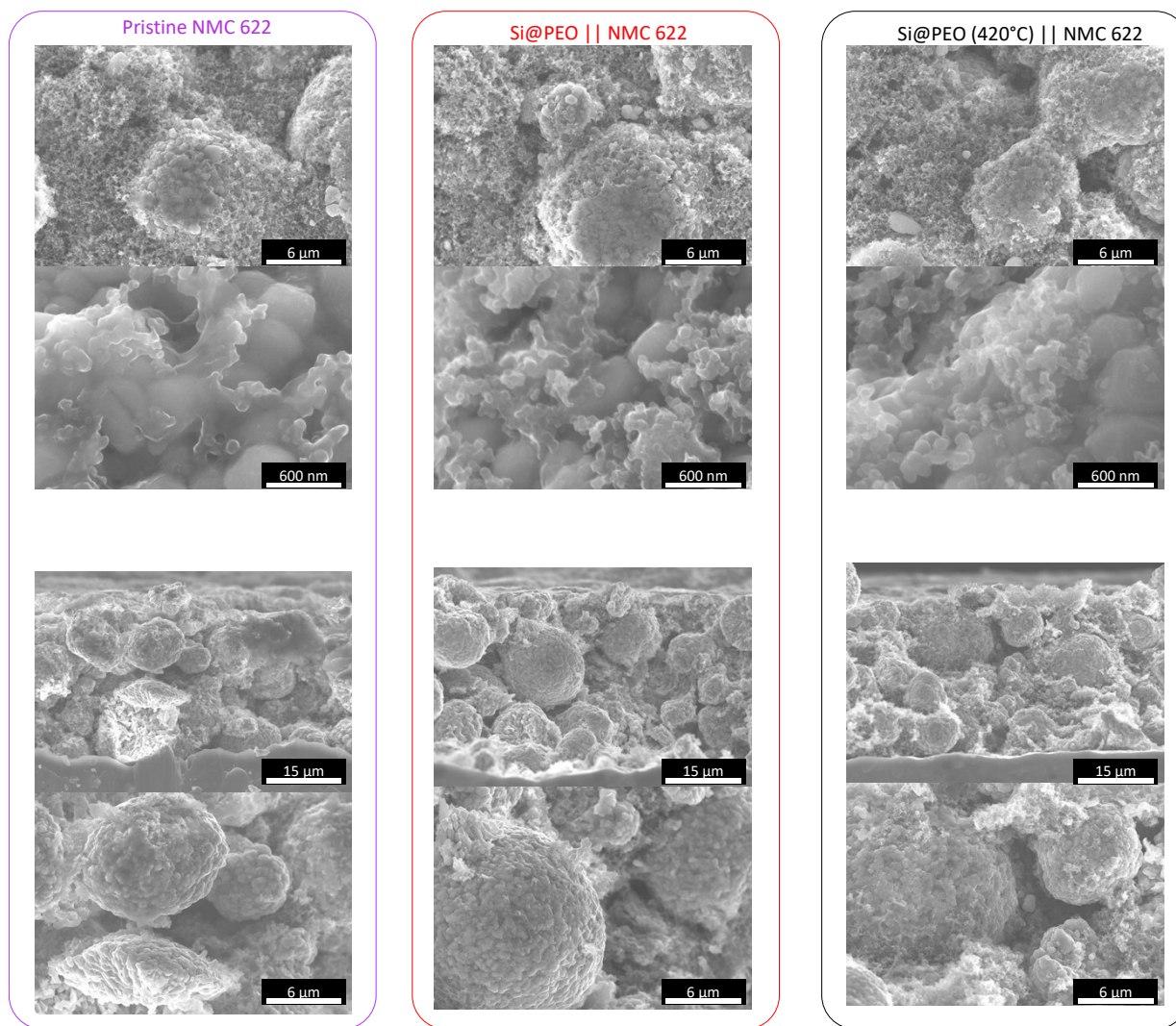
Figure S15. SEM images of the pristine NMC622 cathode (Purple), NMC622 after 1000 cycles against the Si@PEO (red), and Si@PEO (420°C) (black). The top two images show top-down view and the bottom two images are cross-sections.

References.

1.	Mangolini, L.; Thimsen, E.; Kortshagen, U., High-Yield Plasma Synthesis of Luminescent Silicon Nanocrystals. *Nano Lett.* **2005,** *5*, 655.
2.	Wheeler, L. M.; Anderson, N. C.; Palomaki, P. K. B.; Blackburn, J. L.; Johnson, J. C.; Neale, N. R., Silyl Radical Abstraction in the Functionalization of Plasma-Synthesized Silicon Nanocrystals. *Chem. Mater.* **2015,** *27* (19), 6869-6878.
3.	Carroll, G. M.; Schulze, M. C.; Martin, T. R.; Pach, G. F.; Coyle, J. E.; Teeter, G.; Neale, N. R., SiO2 Is Wasted Space in Single-Nanometer-Scale Silicon Nanoparticle-Based Composite Anodes for Li-Ion Electrochemical Energy Storage. *ACS Applied Energy Materials* **2020,** *3* (11), 10993-11001.
4.	Schulze, M. C.; Carroll, G. M.; Martin, T. R.; Sanchez-Rivera, K.; Urias, F.; Neale, N. R., Hydrophobic versus Hydrophilic Interfacial Coatings on Silicon Nanoparticles Teach Us How to Design the Solid Electrolyte Interphase in Silicon-Based Li-Ion Battery Anodes. *ACS Applied Energy Materials* **2021,** *4* (2), 1628-1636.
5.	Oliver, W. C.; Pharr, G. M., Measurement of hardness and elastic modulus by instrumented indentation: Advances in understanding and refinements to methodology. *J. Mater. Res.* **2004,** *19* (1), 3-20.
6.	Paloukis, F.; Elmasides, C.; Farmakis, F.; Selinis, P.; Neophytides, S. G.; Georgoulas, N., Electrochemical Impedance Spectroscopy study in micro-grain structured amorphous silicon anodes for lithium-ion batteries. *J. Power Sources* **2016,** *331*, 285-292.
7.	Huang, Q.; Loveridge, M. J.; Genieser, R.; Lain, M. J.; Bhagat, R., Electrochemical Evaluation and Phase-related Impedance Studies on Silicon–Few Layer Graphene (FLG) Composite Electrode Systems. *Scientific Reports* **2018,** *8* (1), 1386.
8.	Ratynski, M.; Hamankiewiecz, B.; Krajewski, M.; Boczar, M.; Buchberger, D. A.; Czerwinski, A., Electrochemical Impedance Spectroscopy Characterization of Silicon-Based Electrodes for Li-Ion Batteries. *Electrocatalysis* **2020,** *11* (2), 160-169.
9.	Wood, K. N.; Teeter, G., XPS on Li-Battery-Related Compounds: Analysis of Inorganic SEI Phases and a Methodology for Charge Correction. *ACS Applied Energy Materials* **2018,** *1* (9), 4493-4504.